ADVANCED PHYSICS RESEARCH Open Access
www.advphysicsres.com

Magnetic Ni-Nanoinclusions in VO_2 Thin Films for Broad Tuning of Phase Transition Properties

*Zihao He, Jie Jian, Lizabeth Quigley, Nirali A. Bhatt, James P. Barnard, Claire A. Mihalko, Haohan Wang, Xin Li Phuah, Juanjuan Lu, Xiaoshan Xu, and Haiyan Wang**

Mott insulator VO_2 exhibits an ultrafast and reversible semiconductor-to-metal transition (SMT) near 340 K (67 °C). In order to fulfill the multifunctional device applications, effective transition temperature (T_c) tuning as well as integrated functionality in VO_2 is desired. In this study, multifunctionalities including tailorable SMT characteristics, ferromagnetic (FM) integration, and magneto-optical (MO) coupling, have been demonstrated via metal/VO_2 nanocomposite designs with controlled morphology, i.e., a two-phase Ni/VO_2 pillar-in-matrix geometry and a three-phase Au/Ni/VO_2 particle-in-matrix geometry. Evident T_c reduction of 20.4 to 54.9 K has been achieved by morphology engineering. Interestingly, the Au/Ni/VO_2 film achieves a record-low T_c of 295.2 K (22.2 °C), slightly below room temperature (25 °C). The change in film morphology is also correlated with unique property tuning. Highly anisotropic magnetic and optical properties have been demonstrated in Ni/VO_2 film, whereas Au/Ni/VO_2 film exhibits isotropic properties because of the uniform distribution of Au/Ni nanoparticles. Furthermore, a strong MO coupling with enhanced magnetic coercivity and anisotropy is demonstrated for both films, indicating great potential for optically active property tuning. This demonstration opens exciting opportunities for the VO_2-based device implementation towards smart windows, next-generation optical-coupled switches, and spintronic devices.

1. Introduction

Mott insulators have garnered extensive research interest because of the intrinsic strong electron correlation,[1] which shows great promise in data storage and neuromorphic computing.[2,3] In particular, vanadium dioxide (VO_2), as an intriguing Mott insulator, exhibits an ultrafast and reversible semiconductor-to-metal transition (SMT) at a critical temperature (T_c = 340 K).[4–6] A key feature of the SMT transition of VO_2 is the concomitant phase transformation from a high-temperature rutile phase to a low-temperature monoclinic phase upon cooling.[1,7] Several fascinating characteristics associated with the SMT transition include dramatic optical and electrical switching,[8–10] making VO_2 a promising candidate in smart windows,[11] optical and electrical switches,[12,13] etc. However, relatively high T_c has been a long-standing issue that hinders some of the practical applications of VO_2. Therefore, the approaches of T_c tuning toward room temperature have been extensively explored.[14–19] Among all, strain engineering and metallic doping are widely reported as conventional strategies.[14–16] Recently, novel approaches such as metal-VO_2 nanocomposites and metal-ion intercalation have been reported to achieve broad T_c tuning. T_c can be tailored from 302 to 366 K based on the concept of energy band reconstruction[17,18] and intercalation-induced carrier density change.[19]

High-quality multifunctional materials (e.g., materials with coupling of photons, charge, and spin states of carriers) are desired for future electronic and spintronic devices. Hence, it is attractive to incorporate structural, electronic, magnetic, and other degrees of freedom in Mott insulators. Initially, magnetic susceptibility measurements and theoretical calculations confirm the antiferromagnetic arrangement of spins in monoclinic VO_2 single crystals.[4,20,21] For the purpose of multifunctional integration, early attempts including laser annealing and stoichiometry modulation have demonstrated certain tuning capabilities to achieve the weak ferromagnetism in VO_2 films.[22,23] By introducing intrinsic defects (e.g., oxygen vacancies, V^{3+} defects, and stoichiometric defects), the ferromagnetic (FM) behavior can be switched on and off along with the change of

Z. He, H. Wang
School of Electrical and Computer Engineering
Purdue University
West Lafayette, IN 47907, USA
E-mail: hwang00@purdue.edu
J. Jian, L. Quigley, N. A. Bhatt, J. P. Barnard, C. A. Mihalko, X. L. Phuah, J. Lu, H. Wang
School of Materials Engineering
Purdue University
West Lafayette, IN 47907, USA
H. Wang, X. Xu
Department of Physics and Astronomy
University of Nebraska–Lincoln
Lincoln, NE 68588, USA

The ORCID identification number(s) for the author(s) of this article can be found under https://doi.org/10.1002/apxr.202300031

DOI: 10.1002/apxr.202300031

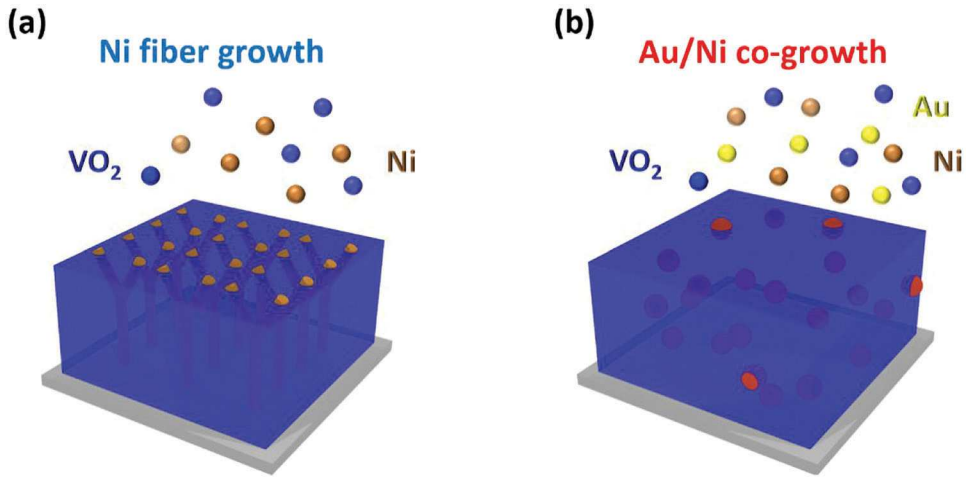

Figure 1. Schematic illustrations of a) two-phase Ni/VO_2 pillar-in-matrix heterostructure and b) three-phase Au/Ni/VO_2 particle-in-matrix heterostructure. Both structures are grown on c-cut sapphire substrates and designed for magnetic and optical applications.

charge carrier density.[22,23] Beyond the intrinsic structural engineering, other heterostructure designs also have demonstrated the feasibility of flexible FM integration.[24–27] For example, the spin polarization in Cr-doped VO_2 film is determined by the dopant concentration,[24] the coercivity enhancement in Ni/VO_2 bilayer is correlated with the substrate selection,[26] and the magnetic anisotropy modulation in VO_2/$(Co/Pt)_2$ heterostructure is realized by internal strain.[27] Furthermore, the interfacial coupling between plasmonic and magnetic components becomes an intriguing direction toward nanophotonic device integration. Such magneto-optical (MO) coupling has been demonstrated in graphene/VO_2 and $[Pt/Co]_2/VO_2/[Co/Pt]_2$,[28,29] whereas the exploration on FM materials/VO_2 systems with the goals of T_c tuning and magnetic incorporation is lacking.

In this study, we propose a novel approach of morphology engineering of metallic nanoinclusions in the metal/VO_2 nanocomposites to accomplish T_c tuning as well as FM integration in the hybrid material framework, using a single-step pulsed laser deposition (PLD) method. As illustrated in **Figure 1**, the conceptual schematics illustrate the proposed morphology engineering in the metal/VO_2 heterostructure: a two-phase Ni/VO_2 pillar-in-matrix geometry and a three-phase Au/Ni/VO_2 particle-in-matrix geometry. Here, Ni is selected as the metal phase because of its FM response at room temperature,[25,30] Au is selected as another metal phase because of its strong plasmonic response and high oxidation resistance property.[17] It is expected that the morphology of the films can be manipulated by lattice matching, diffusion kinetics, and interfacial mixing. Magnetic and optical anisotropy along with MO coupling are probed to evaluate the effect of morphology engineering on the overall multifunctionalities. The proposed two-phase and three-phase metal/VO_2 nanocomposite heterostructures present great potential in combined properties, such as T_c tuning, FM integration, and MO coupling within the VO_2 matrix, and thus open up exciting opportunities for new electronic and optical device designs.

2. Results and Discussion

The crystallinity and microstructures of Ni/VO_2, Au/Ni/VO_2, and pure VO_2 films are systematically characterized using XRD and cross-sectional STEM analysis. All the XRD θ-2θ spectra of the as-deposited films in **Figure 2**a show a distinct VO_2 (020) peak, revealing the textured growth of VO_2 matrices along the b-axis on c-cut sapphire substrates. On the other hand, the VO_2 peak intensities decrease upon coupling with the metal phases, indicating lower film texturing qualities due to the introduced defects and lattice distortion. To further explore the change of strain state in VO_2 matrices, a local XRD θ-2θ spectra near VO_2 (020) peak is shown in Figure S1a, Supporting Information. The VO_2 (020) peaks of Ni/VO_2 and Au/Ni/VO_2 films gradually shift to a smaller angle with respect to the pure VO_2 reference, illustrating gradual tensile strain accumulation along the b-axis upon the introduction of Ni or Au/Ni phase. This observed peak shift could also be attributed to the influence of oxygen vacancies in the lattice.[31] However, based on the XRD analysis and the EDX mapping, there is no obvious NiO peak observed, and Au is a noble metal and will not oxide easily. In addition, the Raman spectra discussed later do not show any obvious Ni-O bonding modes in the sample. From the EDS line scans for the Ni/VO_2 in Figure S2a2, Supporting Information, there is no conclusive trend between the oxygen and the nickel line profile. The line profiles for the Au/Ni/VO_2 film in Figure S2b2, Supporting Information show a clear opposite trend of oxygen intensity and the Au and Ni intensity, i.e., obvious metallic Au/Ni nanostructures in the VO_2 matrix. It is possible the peak shifting observed is likely due to the lattice strain introduced by Ni and Au nanoinclusions, instead of the oxygen vacancies. In addition, the Au (111) peak in the Au/Ni/VO_2 film suggests a preferred distribution of Au nanoparticles within the VO_2 matrix, and a local θ-2θ spectra near Ni (111) peak in Figure S1b, Supporting Information suggests the textured growth of Ni phase along with Au nanoparticles. Comparing the spectra of Ni/VO_2 and Au/Ni/VO_2 films, the introduction of Au nanoparticles can facilitate the textured

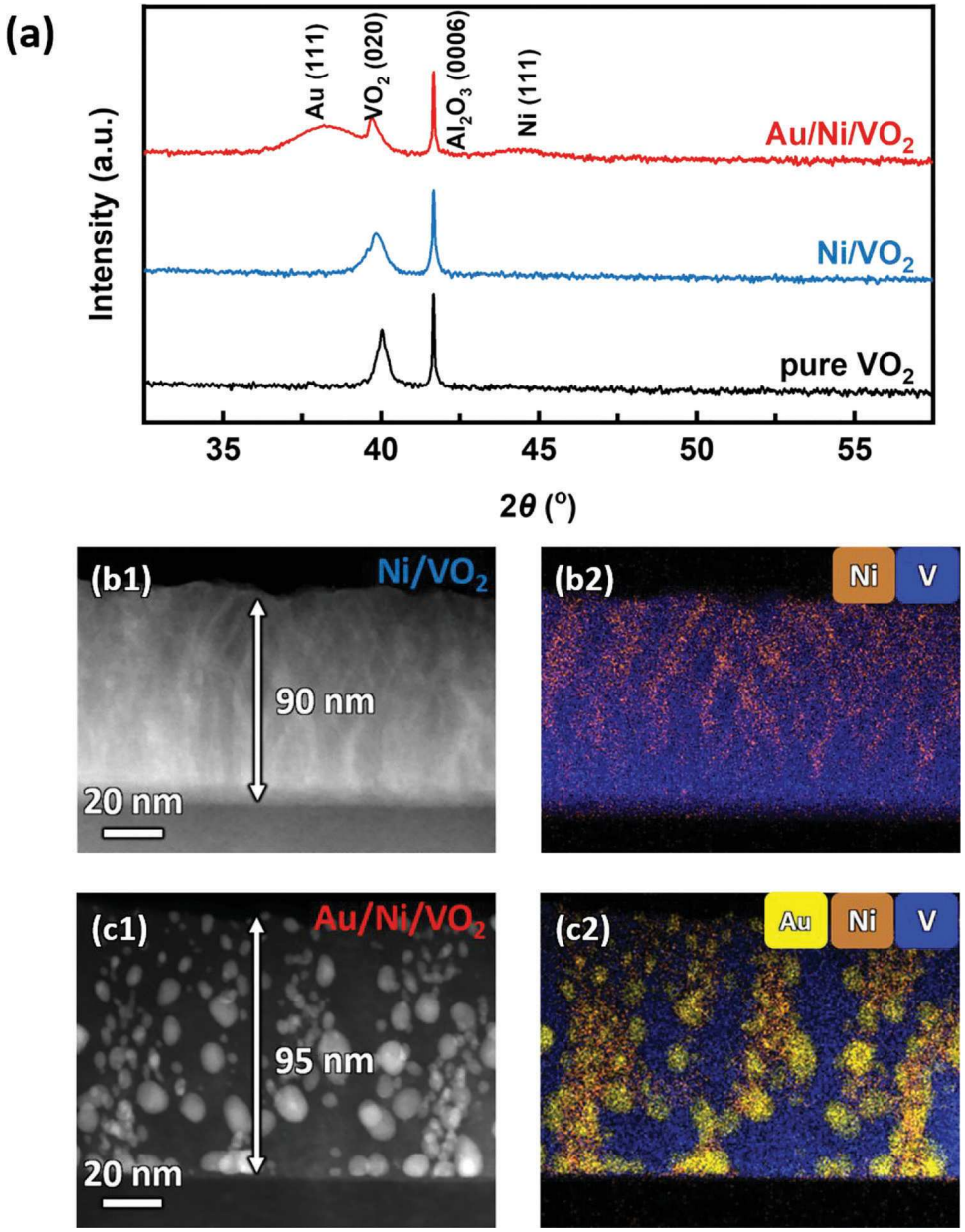

Figure 2. Microstructural characterization. a) XRD θ-2θ spectra of the Ni/VO_2, $Au/Ni/VO_2$, and pure VO_2 films on c-cut sapphire substrates. b1) Cross-sectional STEM micrograph with the corresponding (b2) EDS mapping of the Ni/VO_2 pillar-in-matrix heterostructure. c1) Cross-sectional STEM micrograph with the corresponding c2) EDS mapping of the $Au/Ni/VO_2$ particle-in-matrix heterostructure.

growth of Ni phase in the $Au/Ni/VO_2$ film, while the Ni phase in Ni/VO_2 film tends to distribute in polycrystalline nature. Despite the large lattice mismatch between Au and Ni, Au/Ni bimetallic nanostructures have been previously reported to grow in an Au (111)/Ni (111) epitaxial fashion.[32] The large internal stress in Au/Ni bimetallic nanostructures is compensated by the segregation of Au and the interfacial mixing of two metals.[33,34]

To further explore the microstructure and metal phase distribution within the VO_2 matrix, STEM characterization, and EDS mapping are conducted on Ni/VO_2 and $Au/Ni/VO_2$ films. Both films have a similar thickness of ≈90 nm. However, Figures 2b1,c1 depict two different morphologies upon coupling with metal phases, i.e., a pillar-in-matrix geometry for the Ni/VO_2 heterostructure and a particle-in-matrix geometry for the $Au/Ni/VO_2$ heterostructure. The estimated average ratio of Au to Ni in the $Au/Ni/VO_2$ film was ≈2:1. The Au possesses high oxidation resistance and high thermal stability which allow for the formation of the nanocomposite structures in the film while the kinetic energy of adatoms in the PLD process makes it possible to have Au diffusion onto the substrate. Preferred out-of-plane growth is a result of lower packing energy such as the Au (111) plane, for example.[17] These factors contribute to the formation of the Au/Ni nanoinclusions in VO_2. In the case of Ni/VO_2, there is no preferred orientation for Ni nanofibers, which is a combined

result of diffusion kinetics and the high surface energy of Ni. EDS mapping in Figure 2b2 shows ultra-fine Ni nanofibers within the VO_2 matrix, and the average dimension is ≈3.5 nm. It is noted that Ni nanofibers are surrounded by VO_2 through the TEM foil thickness so that V signal also appears in Figure S3a3, Supporting Information as a background. On the other hand, in the case of Au/Ni/VO_2, Au and Ni phases tend to grow as bimetallic nanoparticles because of the mixing of two metals. The textured growth of Au and Ni phases is the result of the lowest surface energy in (111) plane. EDS mapping in Figure 2c2, Supporting Information shows uniform Au/Ni nanoparticles distribution within the VO_2 matrix, and the average dimension is ≈9 nm. Figure S3b2-4, Supporting Information also confirm the sharp interface between Au/Ni bimetallic nanoparticles and the VO_2 matrix without obvious inter-diffusion.

Raman spectroscopy is carried out to probe the stoichiometry of the as-deposited films and to identify if additional oxides are present. As shown in Figure S4, Supporting Information, all spectra display similar peaks with no obvious peak shift. Specifically, ten peaks labeled in Figure S4, Supporting Information are comparable with the previous reports on phonon modes of VO_2(M1): 142 (B_g), 194 (A_g), 224 (A_g+ B_g), 267 (B_g), 309 (A_g), 338 (A_g), 390 (A_g+ B_g), 499 (A_g), 613 (A_g), 820 (B_g).[35,36] A_g and B_g are phonon modes with different symmetries based on group-theory analysis. V-O modes can be classified into three sets,[37,38] viz., V–O–V bending at Raman shift less than 400 cm^{-1}, V–O–V stretching at Raman shift from 400 to 800 cm^{-1}, and V≐O stretching of distorted octahedra and square pyramids at Raman shift higher than 800 cm^{-1}. The Raman spectra confirm the phase purity and stoichiometry of the as-deposited films, and no Ni–O, Au–Ni–O, or Ni–V–O bonding is observed within the VO_2 matrix. The result agrees with the XRD scan discussed above, i.e., neither NiO (111) nor NiO (002) are noticeable in the θ-2θ spectra. Additionally, the Raman signals are strengthened for Au/Ni/VO_2 film, indicating the surface plasmon enhancement due to Au/Ni nanoparticles.

In order to explore the SMT characteristics tuning of Ni/VO_2 and Au/Ni/VO_2 films, the temperature-dependent electrical resistivity is acquired using the four-point probe method. Figure S5, Supporting Information shows the absolute resistivity plots and **Figure 3**a presents the normalized electrical resistivity, $\rho = \rho(T)/\rho(200\ K)$, of the as-deposited films as a function of temperature. An evident Tc decrease of VO_2 is noted upon coupling with the metal phases. Specifically, Tc reduces by 20.4 K (Ni/VO_2) and 54.9 K (Au/Ni/VO_2) compared to that of the pure VO_2 reference. Oxygen vacancies can also result in a slower SMT and lower T_c due to the valence change of the V ions. In these films, however, when comparing the VO_2 (020) XRD peak intensity for each film, the film quality remains the same evidenced by the similar peak intensity and width, which suggests that oxygen vacancies might not be the main reason for the T_c tuning observed. In particular, the Au/Ni/VO_2 film accomplishes a record-low T_c of 295.2 K (22.2 °C), which demonstrates a more drastic downward T_c tuning compared to the Au/VO_2 and Pt/VO_2 nanocomposite designs in previous studies. The observed T_c tuning of the metal-VO_2 nanocomposites could be facilitated at the metal-VO_2 interfaces and is attributed to the reconstruction of the energy band structure, caused by the formation of a Schottky junction, as previously reported in the VO_2-Au system.[17] This reconstruction results in an increase in the electron density near the phase boundary in the VO_2. This causes a reduction of the coulomb energy barrier thus reducing the temperature required for phase transition.[17,18] To study other SMT characteristics (i.e., transition amplitude (ΔA), transition sharpness (ΔT), and the width of thermal hysteresis (ΔH)), the derivative of $log_{10}(\rho)$ versus temperature of each sample is calculated, as presented in Figure 3b,c,d. Based on these plots, the comparison of ΔT and ΔH is summarized in Figure 3e. The SMT characteristics of the Ni/VO_2 film are very similar to the pure VO_2 counterpart, indicating that high film quality is maintained upon Ni nanofiber incorporation. On the contrary, the Au/Ni/VO_2 film undergoes a nonuniform phase transition, as characterized by the deteriorated amplitude, broad transition width, and wide thermal hysteresis. The decrease of ΔA and the increase of ΔT are related to the reduced film crystallinity and the escalated defect density.[39] The increase of ΔH implies more interfacial energy for switching, which is possibly due to the high density of vertical grain boundaries in VO_2 matrix upon coupling with Au/Ni nanoparticles.[40] In addition, the temperature-dependent electrical resistivity is acquired at different magnetic fields to probe the effect of Ni nano-inclusions on T_c tuning, as illustrated in Figure S6, Supporting Information. A magnetic field up to 9 T is applied along the OP direction. Interestingly, a minor T_c decrease (less than 1 K) is recorded in Ni/VO_2 and Au/Ni/VO_2 films at 9 T. A previous report on magnetic field-induced SMT transition shows T_c ≈100 K at 500 T applied magnetic field in W-doped VO_2.[41] To summarize the T_c tuning effect of the metal phases, both Ni/VO_2 and Au/Ni/VO_2 films demonstrate significant downward T_c tuning, and a T_c of 295.2 K (22.2 °C) slightly below room temperature is achieved in Au/Ni/VO_2 film.

Considering the ferromagnetism induced by Ni nanostructures at room temperature, it is of interest to probe the FM response of Ni/VO_2 and Au/Ni/VO_2 films. The magnetic field up to 3 T is applied either parallel (IP) or perpendicular (OP) to the film surface to investigate the magnetic anisotropy. As illustrated in the room temperature magnetic hysteresis (*M*–*H*) loops (**Figure 4**a1.b1), Ni/VO_2 and Au/Ni/VO_2 films exhibit evident FM response in both IP and OP directions. The low field *M*-*H* loops between ±200 Oe are plotted in Figure 4a2,b2 to decipher the coercivity (H_C). As a comparison, the Au/Ni/VO_2 film does not reveal a clear anisotropy in terms of the coercivity, while the Ni/VO_2 film exhibits much stronger coercivity in the IP direction. The H_C for Ni/VO_2 film varies from 47 Oe (OP) to 89 Oe (IP), indicating a two-fold increase. It is obvious that the morphologies of the metal phases play a role in tuning magnetic anisotropy. Specifically, a strong spin coupling is expected along the c-axis for the pillar-in-matrix heterostructure, which is confirmed by an easy switch along the OP direction in Ni/VO_2 film. In contrast, comparable spin coupling behavior along the IP and OP directions is expected for the particle-in-matrix heterostructure owing to the uniform particle distribution, which is confirmed by the isotropic FM response in Au/Ni/VO_2 film. In addition, *M*-*H* loops at 10 K are presented in Figure S7, Supporting Information. The magnetic anisotropy is maintained under low temperature, whereas the FM response is strengthened because of a stronger spin polarization and less thermal fluctuation.

Furthermore, the FM response can be manipulated by the excitation of surface plasmons, which is known as MO coupling. Such MO coupling is analyzed by collecting the change

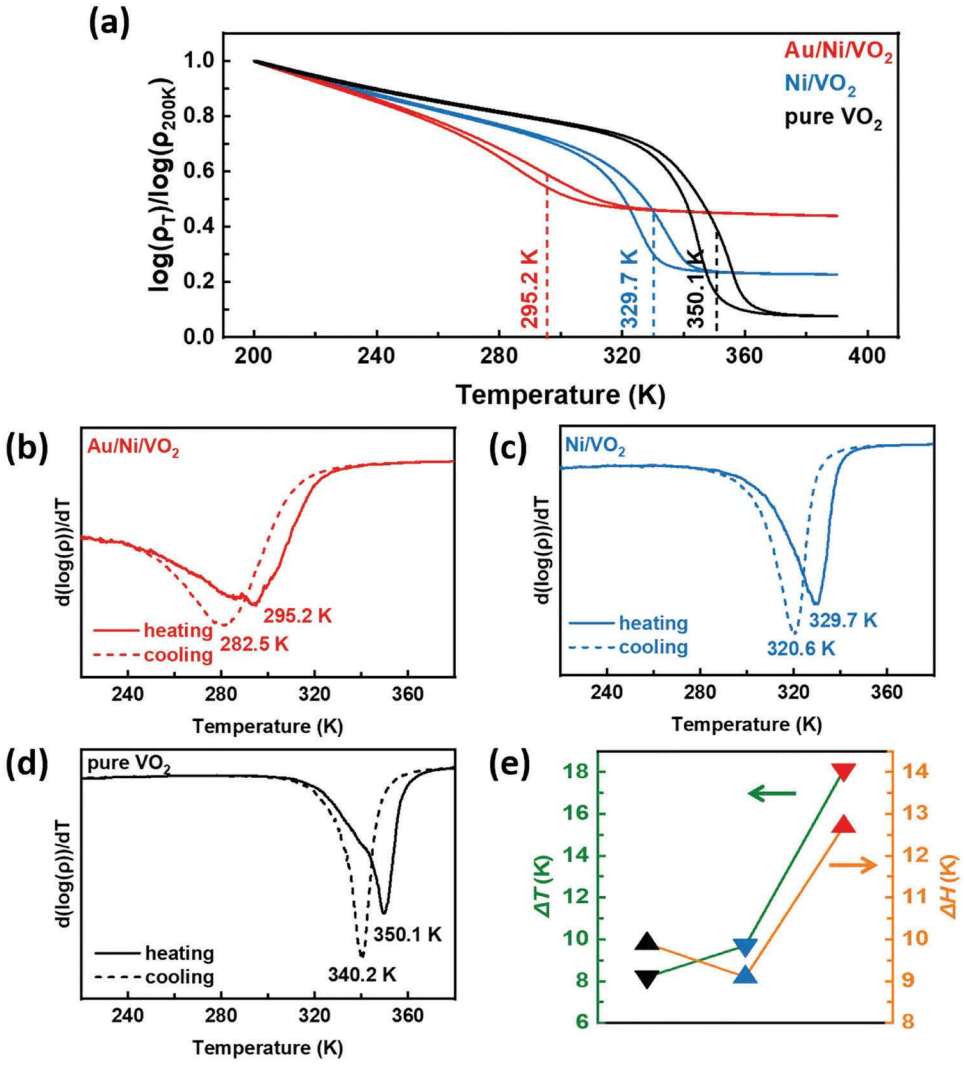

Figure 3. Electrical transport characterization. a) Normalized resistivity-temperature switching plots and the corresponding b–d) resistivity switching rates of the Ni/VO_2, $Au/Ni/VO_2$, and pure VO_2 films, respectively. e) The comparison of ΔT and ΔH of the abovementioned structures. The T_c of both Ni/VO_2 and $Au/Ni/VO_2$ films shift downwards compared to the pure VO_2 film.

of spin polarization upon optical stimulus. Room temperature Kerr rotation is acquired in two geometries, i.e., P-MOKE and L-MOKE. Since both Ni and Au have the broad plasmonic resonance to cover the laser frequency (i.e., ≈450 nm for Ni,[42] ≈700 nm for Au,[43] and 632 nm for He-Ne laser), the excitation of localized surface plasmon resonance (LSPR) is expected at the nanodomain interface when the laser impinges on the sample surface. The weakly aligned FM spins are consequently polarized towards the LSPR-induced magnetic field. As illustrated in Figure S8a2,b2, Supporting Information, only P-MOKE is recorded for the Ni/VO_2 and $Au/Ni/VO_2$ films, and there is no obvious signal for L-MOKE in either sample (Figure S8a1,b1, Supporting Information). The result reveals a strong anisotropic MO coupling along the OP direction for both films. Compared to the FM response in *M*–*H* loops, the coercivity opening during the Kerr measurement is marked with black arrows, illustrating a drastic enhancement of Kerr rotation upon LSPR excitation. The H_C for Ni/VO_2 film increases from 47 Oe (Figure 4a2) to 351 Oe (Figure S9a2,b2, Supporting Information), and the H_C for $Au/Ni/VO_2$ film increases from 97 Oe (Figure 4b2) to 323 Oe (Figure S9a2,b2, Supporting Information). Interestingly, the $Au/Ni/VO_2$ film exhibits a slightly stronger MOKE response compared to that of the Ni/VO_2 film. The enhanced coupling in $Au/Ni/VO_2$ film is possibly due to the particle nature of the Au/Ni phase, which offers a greater degree of interfacial coupling and spin canting at the $Au/Ni/VO_2$ interface.

In order to evaluate the light-matter interaction and the tuning effects for the Ni/VO_2, $Au/Ni/VO_2$, and pure VO_2 films, the dielectric response of all films are analyzed using angular-dependent spectroscopic ellipsometry. First, by considering the as-deposited films as isotropic absorbing layers, the dielectric permittivity ϵ' (real part) is compared at 25 and 100 °C to probe the change of charge carrier density, as illustrated in **Figure 5**a,b. Overall, the optical response switches from low-temperature

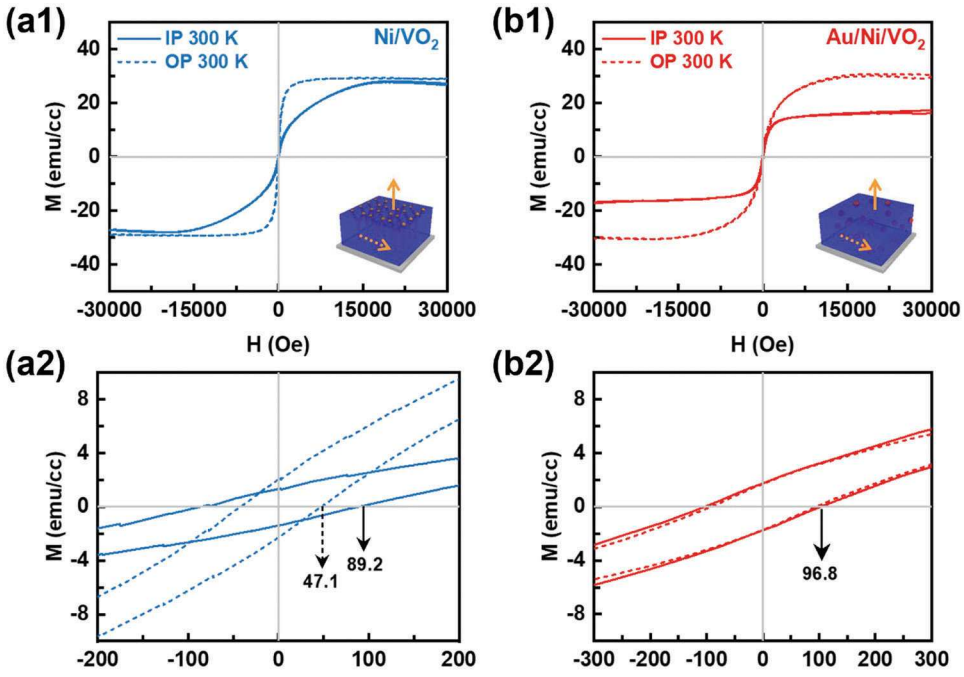

Figure 4. Magnetic characterization. a1) Room-temperature magnetic hysteresis loops and the corresponding a2) enlarged displays of the Ni/VO_2 pillar-in-matrix heterostructure. b1) Room-temperature magnetic hysteresis loops and the corresponding b2) enlarged displays of the $Au/Ni/VO_2$ particle-in-matrix heterostructure. Low field *M–H* loops between ±200 Oe are plotted in a2) and b2) to decipher the coercivity (H_C) in both IP and OP directions.

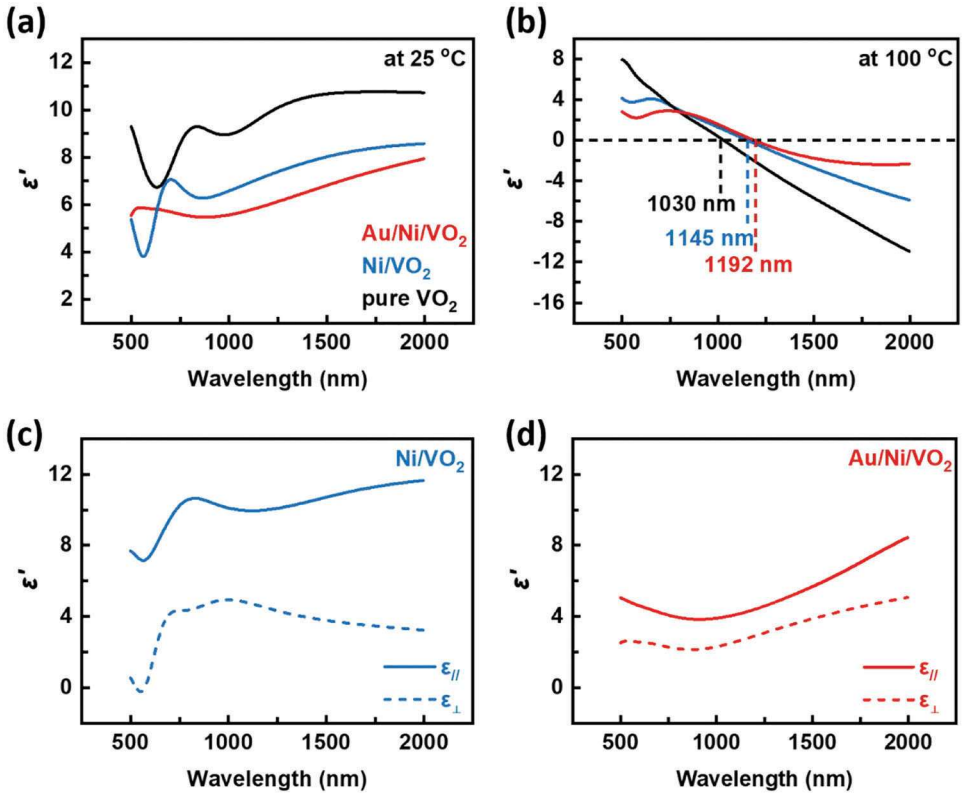

Figure 5. Optical characterization. The real-part dielectric permittivity ϵ' of the Ni/VO_2, $Au/Ni/VO_2$, and pure VO_2 films a) at 25 °C and b) at 100 °C, respectively. The inset values represent the ENZ wavelengths correspondingly. Considering the anisotropic optical response, IP ($\epsilon_{//}$) and OP ($\epsilon_{\perp}$) permittivity of c) the Ni/VO_2 pillar-in-matrix heterostructure and (d) the $Au/Ni/VO_2$ particle-in-matrix heterostructure.

dielectric behavior (positive ϵ') to high-temperature metallic behavior (negative ϵ'), indicating a good agreement with the electrical resistivity switching discussed in the previous section (Figure 3). Moreover, the decrease of ϵ' at room temperature (Figure 5a) in the Ni/VO_2 and $Au/Ni/VO_2$ films is correlated with the metal phase incorporation. However, both Ni/VO_2 and $Au/Ni/VO_2$ films remain effectively dielectric (positive ϵ') at room temperature because the VO_2 matrix plays a dominant role. On the other hand, Figure 5b displays a systematic tuning of the epsilon-near-zero (ENZ) wavelength, in which the redshift of plasmon frequency is related with the decrease of charge carrier density after phase transition. Next, the anisotropic dielectric response of Ni/VO_2 and $Au/Ni/VO_2$ films is retrieved from uniaxial models, i.e., the dielectric tensor is separated into IP ($\epsilon_{//}$) and OP ($\epsilon_{\perp}$) terms. For the Ni/VO_2 film (Figure 5c), an evident optical anisotropy between IP and OP is observed, and it becomes more significant at high wavelengths. Such anisotropic behavior in the Ni/VO_2 film is attributed to a more metallic nature (i.e., Ni nanofibers) of the vertical geometry. On the contrary, the anisotropy is much weaker for the $Au/Ni/VO_2$ film (Figure 5d), which is attributed to the isotropic distribution of Au/Ni nanoparticles within the VO_2 matrix. To summarize, the dielectric permittivity study confirms that the anisotropic nature of the Ni/VO_2 film and the isotropic nature of the $Au/Ni/VO_2$ film both effectively extend to the optical domain.

Previous studies have demonstrated strain engineering and the consequent magnetic modulation in Ni/VO_2 bilayers.[26,44] The effect of metallic doping (e.g., Ni/W-doped VO_2) on the Ni/VO_2 morphology was also discussed.[45] In addition, the Ni/VO_2 nanoflower structure demonstrated a potential application in Li–S batteries with a strong adsorption acceleration effect.[46] However, a systematic study on the SMT characteristics tuning via FM phase integration is lacking, which is potentially favorable for room temperature VO_2-based electronic and photonic applications. Here, the Ni/VO_2 and $Au/Ni/VO_2$ nanocomposite designs demonstrate a simple approach for effective T_c tuning as well as magnetic and optical tuning via morphology engineering. The novelty of this study includes: 1) taking advantage of the morphology engineering, T_c effectively reduces by 20.4 K in Ni/VO_2 with pillar-in-matrix heterostructure and 54.9 K in $Au/Ni/VO_2$ with particle-in-matrix heterostructure, compared to that of the pure VO_2 reference. Notably, $Au/Ni/VO_2$ film accomplishes a record-low T_c of 295.2 K (22.2°C), which is slightly below room temperature (25 °C); 2) high-quality film of metal/VO_2 nanocomposite design avoids the deterioration of SMT characteristics, indicating a major advantage compared to metal-doping and strain engineering approaches;[14,47,48] 3) the magnetic and optical anisotropy, including spin polarization and charge carrier distribution, can be systematically manipulated via morphology engineering, and significant enhancement of MO coupling is achieved. The integration of magnetic nano-inclusions into the VO_2 matrix in a controlled morphology opens up exciting opportunities for the device implementation towards sensors, memristive switches, surface plasmon-enhanced thermochromic smart windows, etc. Other magnetic candidates, such as Co/VO_2, Fe/VO_2, and other multiphase designs are worth exploring towards versatile metal/VO_2 nanocomposite frameworks for property tuning and magnetic-optical-electrical coupling schemes.

3. Conclusion

In summary, significant T_c tuning as well as tailorable magnetic and optical properties have been demonstrated in magnetic Ni/VO_2 and $Au/Ni/VO_2$ nanocomposite designs via morphology engineering. Ni nanofibers tend to grow vertically as a pillar-in-matrix geometry, whereas Au/Ni nanoparticles are uniformly distributed in the VO_2 matrix as a particle-in-matrix geometry. T_c effectively reduces by 20.4 K in Ni/VO_2 and 54.9 K in $Au/Ni/VO_2$ compared to that of the pure VO_2 reference. In particular, the $Au/Ni/VO_2$ film accomplishes a T_c of 295.2 K (22.2 °C) slightly below room temperature. The change in film morphology is also correlated with the property tuning. The Ni/VO_2 film reveals an obvious OP anisotropy in the magnetic and optical properties. In contrast, the Au/Ni/VO2 film exhibits an isotropic response due to a uniform nanoparticle distribution. Furthermore, a strong MO coupling with enhanced magnetic coercivity and anisotropy is observed for both films, indicating optically active film surfaces. Such nanocomposite designs are worth exploring in other Mott-insulating oxides for flexible integration of magnetic properties, which hold great promise for next-generation photonic and spintronic devices integrated with Mott transition properties.

4. Experimental Section

Composite Thin Film Deposition: All films were deposited using pulsed laser deposition (PLD) with a KrF excimer laser (λ = 248 nm). The pure VO_2 film was deposited with a V_2O_5 target, Ni/VO_2 nanocomposite film was deposited with a 20 at% Ni/V_2O_5 composite target, and $Au/Ni/VO_2$ nanocomposite film was deposited by attaching an Au foil piece on top of a 20 at% Ni/V_2O_5 composite target. All films were deposited on c-cut sapphire substrates for 30 min under the same deposition conditions: substrate temperature of 500 °C, oxygen pressure of 10 mTorr, laser repetition rate of 2 Hz, and approximate laser fluence of 3 J cm^{-1}.[

Microstructural Characterization: The crystallinity and microstructures of Ni/VO_2, $Au/Ni/VO_2$, and pure VO_2 films were characterized using X-ray diffraction (XRD), scanning transmission electron microscopy (STEM), and Energy-dispersive X-ray spectroscopy (EDS). XRD θ–2θ scans were conducted using a PANalytical Empyrean X-ray diffractometer with Cu K_α radiation (λ = 0.154 nm). Both STEM and EDS were acquired using Thermo Scientific TALOS F200X operated at 200 kV. Cross-sectional TEM specimens were prepared by standard grinding, dimpling, and precision ion polishing using Gatan PIPS 695 operated at 5 keV.

Electrical Characterization: The electrical resistivity switching of Ni/VO_2, $Au/Ni/VO_2$, and pure VO_2 film were investigated using a physical property measurement system (PPMS DynaCool, Quantum Design). The switching behavior of all samples was characterized in the in-plane direction by a standard four-point-probe configuration, a schematic of which is shown in Figure S9, Supporting Information. Au contacts were deposited using DC sputtering before the measurement. The temperature was swept 200 K → 390K → 200 K at 2 K/min. The switching behavior was also investigated at a magnetic field up to 9 T along out-of-plane direction.

Magnetic and Magneto-Optic Property Characterization: The magnetic properties of all films were investigated using a vibrating sample magnetometer in a magnetic property measurement system (MPMS3 SQUID, Quantum Design). The magnetic field up to 3 T was applied either parallel (in-plane, IP) or perpendicular (out-of-plane, OP) to the film surface to study the magnetic anisotropy. The raw magnetization data was corrected to eliminate potential magnetic remanence, high-field error, and sample geometry effect.

The room temperature magneto-optic Kerr effect (MOKE) was analyzed using a home-built MOKE system. An intensity-stabilized He-Ne laser (λ = 632 nm) was applied as the probing laser. The magnetic field was applied

from −3500 Oe to 3500 Oe in the polar geometry, and from −7000 Oe to 7000 Oe in the longitudinal geometry. In the polar geometry (P-MOKE, magnetic field is perpendicular to the film surface), the reflected light was separated from the normal incident light by a 50% beam splitter. In the longitudinal geometry (L-MOKE, magnetic field is parallel to the film surface), the in-plane polarized laser impinges at ≈30° from the sample normal.

Optical and Raman Characterization: The optical dielectric permittivity of all films was analyzed using a spectroscopic ellipsometer (RC2 ellipsometer, J.A. Woollam). The incident angles were set from 55° to 75°, and the spectrum range was set from 500 nm to 2000 nm. The dielectric permittivity was calculated by modeling appropriate oscillators using two ellipsometric parameters psi (Ψ) and delta (Δ). The model was assumed to be isotropic for Au/Ni/VO_2 and pure VO_2 film, and to be anisotropic for Ni/VO_2 film owing to the Ni nanofiber distribution. The room temperature (25 °C) permittivity was constructed using one Tauc-Lorentz oscillator and two Lorentz oscillators, and the elevated temperature (100 °C) permittivity was constructed using one Drude oscillator and one Lorentz oscillator. Raman spectra were acquired using a Raman micro-spectrometer (Renishaw inVia) in a confocal excitation and collection configuration. All spectra were collected using a 532 nm laser beam and an NA = 0.9 objective.

Supporting Information

Supporting Information is available from the Wiley Online Library or from the author.

Acknowledgements

The authors acknowledged the support from the U.S. National Science Foundation (DMR-1809520 for thin film deposition and DMR-2016453 for high-resolution STEM characterization). N.A.B. acknowledges the Purdue Andrews fellowship support and Sandia National Laboratory Diversity Fellowship support. L.Q. acknowledges the Purdue Doctoral Fellowship support and the Sandia National Laboratory Diversity Fellowship support. J.L. and H.W. acknowledge the support from the U.S. Department of Energy (DOE), Office of Science, Basic Energy Sciences (BES) under Award DE-SC0020077. H.H.W. and X.X. acknowledge the support from the U.S. DOE BES under Award DE-SC0019173.

Conflict of Interest

The authors declare no conflict of interest.

Author Contributions

The project was conceived and led by Z.H. and H.W. Z.H., and J.J. contributed to the sample fabrication, XRD, STEM, EDS, and electrical transport characterization. L.Q. and J.B. contributed to the magnetic characterization. N.A.B. contributed to the TEM sample preparation. H.H.W. and X.X. contributed to the MOKE measurements. X.P. contributed to the target preparation. J.L. contributed to the optical characterization. The manuscript was drafted and revised by Z.H. and H.W. All authors have revised and approved the final version of the manuscript.

Data Availability Statement

The data that support the findings of this study are available in the supplementary material of this article.

Keywords

VO_2, magnetic properties, optical properties, transition temperature

Received: March 14, 2023
Revised: June 5, 2023
Published online: September 22, 2023

[1] A. Zylbersztejn, N. F. Mott, *Phys. Rev. B* **1975**, *11*, 4383.
[2] M. D. Pickett, G. Medeiros-Ribeiro, R. S. Williams, *Nat. Mater.* **2012**, *12*, 114.
[3] Y. Zhou, S. Ramanathan, *Proc. IEEE* **2015**, *103*, 1289.
[4] F. J. Morin, *Phys. Rev. Lett.* **1959**, *3*, 34.
[5] J. B. Goodenough, *J. Solid State Chem.* **1971**, *3*, 490.
[6] M. Imada, A. Fujimori, Y. Tokura, *Rev. Mod. Phys.* **1998**, *70*, 1039.
[7] V. Eyert, *Ann. Phys.* **2002**, *11*, 650.
[8] G. Stefanovich, A. Pergament, D. Stefanovich, *J. Phys. Condens. Matter* **2000**, *12*, 8837.
[9] M. M. Qazilbash, M. Brehm, B. G. Chae, P. C. Ho, G. O. Andreev, B. J. Kim, S. J. Yun, A. V. Balatsky, M. B. Maple, F. Keilmann, H. T. Kim, D. N. Basov, *Science* **2007**, *318*, 1750.
[10] M. Liu, H. Y. Hwang, H. Tao, A. C. Strikwerda, K. Fan, G. R. Keiser, A. J. Sternbach, K. G. West, S. Kittiwatanakul, J. Lu, S. A. Wolf, F. G. Omenetto, X. Zhang, K. A. Nelson, R. D. Averitt, *Nature* **2012**, *487*, 345.
[11] Z. Chen, Y. Gao, L. Kang, J. Du, Z. Zhang, H. Luo, H. Miao, G. Tan, *Sol. Energy Mater. Sol. Cells* **2011**, *95*, 2677.
[12] H. Wang, X. Yi, Y. Li, *Opt. Commun.* **2005**, *256*, 305.
[13] A. Crunteanu, J. Givernaud, J. Leroy, D. Mardivirin, C. Champeaux, J. C. Orlianges, A. Catherinot, P. Blondy, *Sci. Technol. Adv. Mater.* **2010**, *11*, 6.
[14] T. D. Manning, I. P. Parkin, C. Blackman, U. Qureshi, *J. Mater. Chem.* **2005**, *15*, 4560.
[15] J. Jeong, N. Aetukuri, T. Graf, T. D. Schladt, M. G. Samant, S. S. P. Parkin, *Science* **2013**, *339*, 1402.
[16] J. Jian, X. Wang, L. Li, M. Fan, W. Zhang, J. Huang, Z. Qi, H. Wang, *ACS Appl. Mater. Interfaces* **2017**, *9*, 5319.
[17] J. Jian, X. Wang, S. Misra, X. Sun, Z. Qi, X. Gao, J. Sun, A. Donohue, D. Gen Lin, V. Pol, J. Youngblood, H. Wang, L. Li, J. Huang,, H. Wang, *Adv. Funct. Mater.* **2019**, *29*, 1903690.
[18] Z. He, J. Jian, S. Misra, X. Gao, X. Wang, Z. Qi, B. Yang, D. Zhang, X. Zhang, H. Wang, *Nanoscale* **2020**, *12*, 17886.
[19] Z. He, Z. Qi, B. Yang, P. Lu, J. Shen, N. R. Dilley, X. Zhang, H. Wang, *Nano Lett.* **2023**, *23*, 1119.
[20] N. F. Mott, *Philos. Mag.* **1961**, *6*, 287.
[21] J. P. Pouget, H. Launois, J. P. O'haenens, P. Merenda, T. M. Rice, *Phys. Rev. Lett.* **1975**, *35*, 873.
[22] T. H. Yang, S. Nori, S. Mal, J. Narayan, *Acta Mater.* **2011**, *59*, 6362.
[23] R. Molaei, R. Bayati, S. Nori, D. Kumar, J. T. Prater, J. Narayan, *Appl. Phys. Lett.* **2013**, *103*, 252109.
[24] K. G. West, J. Lu, L. He, D. Kirkwood, W. Chen, T. Paul Adl, M. S. Osofsky, S. B. Qadri, R. Hull, S. A. Wolf, K. West, J. Lu, L. He, D. Kirkwood, R. Hull, S. Wolf, W. Chen, T. Adl, M. Osofsky, S. Qadri, *J. Supercond. Nov. Magn.* **2008**, *21*, 87.
[25] G. M. Foley, S. R. Singamaneni, J. Prater, J. Narayan, *MRS Adv.* **2016**, *1*, 3409.
[26] J. Lauzier, L. Sutton, J. De La Venta, *J. Appl. Phys.* **2017**, *122*, 173902.
[27] G. Wei, X. Lin, Z. Si, N. Lei, Y. Chen, S. Eimer, W. Zhao, *Appl. Phys. Lett.* **2019**, *114*, 012407.
[28] B. Yu, T. Tang, R. Wang, S. Qiao, Y. Li, C. Li, J. Shen, X. Huang, Y. Cao, *J. Magn. Magn. Mater.* **2021**, *530*, 167946.
[29] X. Fan, G. Wei, X. Lin, X. Wang, Z. Si, X. Zhang, Q. Shao, S. Mangin, E. Fullerton, L. Jiang, W. Zhao, *Matter* **2020**, *2*, 1582.
[30] J. M. Shaw, H. T. Nembach, T. J. Silva, *J. Appl. Phys.* **2010**, *108*, 093922.
[31] Z. Li, Y. Ren, L. Mo, C. Liu, K. Hsu, Y. Ding, X. Zhang, X. Li, L. Hu, D. Ji, G. Cao, *ACS Nano.* **2020**, *14*, 5581.

[32] M. Tsuji, D. Yamaguchi, M. Matsunaga, K. Ikedo, *Cryst. Growth Des.* **2011**, *11*, 1995.
[33] B. Legrand, G. Tréglia, J. Gay, B. Aufray, *Phys. Rev. B* **1999**, *59*, 10910.
[34] S. Labat, F. Bocquet, B. Gilles, O. Thomas, *Scr. Mater.* **2004**, *50*, 717.
[35] P. Schilbe, *Phys. B Condens. Matter* **2002**, *316-317*, 600.
[36] K. Shibuya, A. Sawa, *J. Appl. Phys.* **2017**, *122*, 015307.
[37] C. Marini, E. Arcangeletti, D. Di Castro, L. Baldassare, A. Perucchi, S. Lupi, L. Malavasi, L. Boeri, E. Pomjakushina, K. Conder, P. Postorino, *Phys. Rev. B – Condens. Matter Mater. Phys.* **2008**, *77*, 235111.
[38] F. D. Hardcastle, I. E. Wachs, *J. Phys. Chem.* **1991**, *95*, 5031.
[39] D. Brassard, S. Fourmaux, M. Jean-Jacques, J. C. Kieffer, M. A. El Khakani, *Appl. Phys. Lett.* **2005**, *87*, 051910.
[40] J. Narayan, V. M. Bhosle, *J. Appl. Phys.* **2006**, *100*, 103524.
[41] Y. H. Matsuda, D. Nakamura, A. Ikeda, S. Takeyama, Y. Suga, H. Nakahara, Y. Muraoka, *Nat. Commun.* **2020**, *11*, 1.
[42] J. Chen, P. Albella, Z. Pirzadeh, P. Alonso-González, F. Huth, S. Bonetti, V. Bonanni, J. Åkerman, J. Nogués, P. Vavassori, A. Dmitriev, J. Aizpurua, R. Hillenbrand, J. Chen, P. Albella, P. Alonso-González, F. Huth, P. Vavassori, R. Hillenbrand, J. Aizpurua, Z. Pirzadeh, V. Bonanni, A. Dmitriev, J. Åkerman, S. Bonetti, J. Nogués, *Small* **2011**, *7*, 2341.
[43] Q. H. Wei, K. H. Su, S. Durant, X. Zhang, *Nano Lett.* **2004**, *4*, 1067.
[44] Y. Yang, B. Hong, H. Huang, Z. Luo, C. Gao, C. Kang, X. Li, *J. Mater. Sci. Mater. Electron.* **2018**, *29*, 2561.
[45] L. Sutton, A. Blehm, J. Lauzier, K. Malone, G. Smith, M. Singh, J. de la Venta, *J. Supercond. Nov. Magn.* **2020**, *33*, 2493.
[46] D. Zhang, R. Gu, F. Y. Lan, W. Y. Guo, C. W. Deng, Q. J. Xu, H. X. Li, Y. L. Min, *ACS Sustainable Chem. Eng.* **2021**, *9*, 16251.
[47] N. R. Mlyuka, G. A. Niklasson, C. G. Granqvist, *Appl. Phys. Lett.* **2009**, *95*, 171909.
[48] J. Jian, A. Chen, Y. Chen, X. Zhang, H. Wang, *Appl. Phys. Lett.* **2017**, *111*, 153102.